Faraday Discussions

Cite this: *Faraday Discuss.*, 2020, **221**, 379

PAPER

Challenges in constructing accurate methods for hydrogen transfer reactions in large biological assemblies: rare events sampling for mechanistic discovery and tensor networks for quantum nuclear effects

Nicole DeGregorio and Srinivasan S. Iyengar *

Received 22nd May 2019, Accepted 22nd July 2019
DOI: 10.1039/c9fd00071b

We present two methods that address the computational complexities arising in hydrogen transfer reactions in enzyme active sites. To address the challenge of reactive rare events, we begin with an *ab initio* molecular dynamics adaptation of the Caldeira–Leggett system-bath Hamiltonian and apply this approach to the study of the hydrogen transfer rate-determining step in soybean lipoxygenase-1. Through direct application of this method to compute an ensemble of classical trajectories, we discuss the critical role of isoleucine-839 in modulating the primary hydrogen transfer event in SLO-1. Notably, the formation of the hydrogen bond between isoleucine-839 and the acceptor-OH group regulates the electronegativity of the donor and acceptor groups to affect the hydrogen transfer process. Curtailing the formation of this hydrogen bond adversely affects the probability of hydrogen transfer. The second part of this paper deals with complementing the rare event sampled reaction pathways obtained from the aforementioned development through quantum nuclear wavepacket dynamics. Essentially the idea is to construct quantum nuclear dynamics on the potential surfaces obtained along the biased trajectories created as noted above. Here, while we are able to obtain critical insights on the quantum nuclear effects from wavepacket dynamics, we primarily engage in providing an improved computational approach for efficient representation of quantum dynamics data such as potential surfaces and transmission probabilities using tensor networks. We find that utilizing tensor networks yields an accurate and efficient description of time-dependent wavepackets, reduced dimensional nuclear eigenstates and associated potential energy surfaces at much reduced cost.

Department of Chemistry, Department of Physics, Indiana University, Bloomington, IN 47405, USA. E-mail: iyengar@indiana.edu

I. Introduction

Hydrogen transfer reactions[1–3] are prevalent in a wide range of chemical, biological and materials systems. Yet these are some of the most complex and challenging problems to study from a fundamental perspective. The challenges presented by these problems arise from the following: (a) while the hydrogen transfer step may itself be expected to proceed on a pico-second time-scale, the reorganization of the active-site and other facilitating degrees of freedom that allow such a transfer may occur on a much slower time-regime which in general makes the reactive process a rare event.[4,5] Computing rare events in such complex reactive processes is a great challenge. (b) Due to the light nature of the nuclei involved in the reactive process, on many occasions quantum nuclear effects, including hydrogen tunneling, become important to consider and these are seen through anomalous H/D (primary and sometimes secondary) kinetic isotope effects. (c) Furthermore, when these quantum nuclear degrees of freedom become strongly dependent on the electronic structure, this presents a serious challenge for computation requiring simultaneous treatment of electronic and nuclear motion. (d) In addition, the motion of the active site is almost never strictly decoupled from the reactive event. Thus, strictly speaking, both adiabatic and non-adiabatic limits become relevant in terms of separation of the reactive degrees of freedom, where the coupled dynamics of neighboring light nuclei can sometimes lead to non-traditional secondary kinetic isotope effects; in such cases, coupled treatment of the dynamics becomes essential.

In this publication we outline recent computational developments towards addressing the above listed challenges. The paper is organized as follows: in Section II we present an adaptation of *ab initio* molecular dynamics to allow the treatment of rare events. The method uses the Caldeira–Leggett[6,7] approach from quantum dissipation, and here we present a form of the method that is appropriate for studies where *a priori* information is available with regards to the reactive event (that is, with approximately pre-defined reactant and product states which in this case correspond to pre-defined donor and acceptor groups). The method is applied to the study of the rate-determining hydrogen transfer step (Fig. 1) in the oxidation of linoleic acid by soybean lipoxygenase-1 (SLO-1)[8–27] and the role of the backbone carbonyl group in ILE-839 is discussed with respect to contributions to the reactive process. As noted in ref. 28, on the hydrogen-transfer donor side, the approach allows one to gauge the coupled dynamics associated with secondary hydrogen nuclei to provide a qualitative explanation for anomalous secondary isotope effects from Klinman and

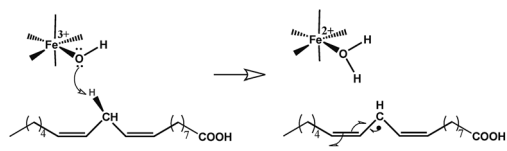

Fig. 1 Hydrogen abstraction is the rate-determining step in the oxidation of linoleic acid by SLO-1.

Rickert.[29] The discussion in Section IIA is classical in terms of treatment of nuclei and the electronic structure is treated on-the-fly with DFT. In Section III we probe quantum nuclear effects in this system. In a previous publication[16] we have treated the problem using quantum wavepacket dynamics on *ab initio* potential energy surfaces that depend on the classical coordinates of the active site atoms, along the biased trajectories discussed in Section IIA. Given the exponential scaling nature of such calculations, especially when the quantum nuclear dimensions are fully correlated with the electronic structure (through a grid-based approach for the quantum dynamics), in Section III we provide a treatment of the quantum nuclear effects using tensor networks. We have shown this approach to work accurately for smaller hydrogen transfer systems[30] and here we write down the quantum mechanical wavepacket, eigenstates and potential energy surface as matrix-product-states[30–32] and the transmission probabilities are recovered through the action on such matrix-product-states to provide lower scaling methods in agreement with previous wavepacket studies. Furthermore, tensor network descriptions for the potential surface greatly reduce the computational effort and will in future be used for quantum nuclear wavepacket dynamics in such complex systems. Conclusions are given in Section IV. Appendices A and B complement the discussion in Sections IIA and III.

II. Computing rare events in complex assemblies through *ab initio* molecular dynamics

We introduce a Caldeira–Leggett-type[6,7] system-bath Hamiltonian for a collective electron nuclear system coupled to a set of bath degrees of freedom. We use this to compute rare events in the hydrogen transfer step of the catalytic oxidation of linoleic acid by SLO-1. We begin our discussion by introducing a Car–Parrinello-like[33] extended Hamiltonian with Lagrangian constraints, that uses atom-centered electronic basis functions and single-particle density matrices and is hence based on the atom-centered density matrix (ADMP) formalism:[34–40]

$$\mathscr{H}_S = \frac{1}{2}\mathrm{Tr}\left[\mathbf{V}^T\mathbf{M}\mathbf{V}\right] + \frac{1}{2}\mathrm{Tr}\left(\left[\mu^{\frac{1}{4}}\mathbf{W}\mu^{\frac{1}{4}}\right]^2\right) + E(\mathbf{R},\mathbf{P}) + \mathrm{Tr}[\mathbf{\Lambda}(\mathbf{PP}-\mathbf{P})]. \quad (1)$$

Here $\mathbf{M}$, $\mathbf{R}$, $\mathbf{V}$ are the nuclear masses, atomic positions and velocities. The single-particle electronic density matrix, density matrix velocity, and the fictitious inertia tensor[35] for the electronic degrees of freedom are $\mathbf{P}$, $\mathbf{W}$, and μ respectively. The function $E(\mathbf{R},\mathbf{P})$ is the *ab initio* potential energy function assumed here to have a QM/MM form where the QM portion is at a single particle level of theory such as DFT. The potential energy, $E(\mathbf{R},\mathbf{P})$, is a function of the single-particle electronic density matrix, $\mathbf{P}$ and nuclear positions, $\mathbf{R}$. The last term in eqn (1) imposes constraints on the total number of electrons and on the idempotency of the density matrix using a Lagrangian multiplier matrix $\mathbf{\Lambda}$. See also ref. 40–44 where eqn (1) has been generalized to include post-Hartree–Fock (CCSD) accuracy, on-the-fly, thus providing a Car–Parrinello-like dynamics method with CCSD[40] and MP2 (ref. 43) accuracy, along with on-the-fly basis set extrapolation.[44]

If we now introduce a family of harmonic bath variables, $\tilde{\mathbf{R}}$, external to the system variables, $\mathbf{R}$, with quantities $\tilde{\mathbf{M}}$, $\tilde{\mathbf{R}}$, and $\tilde{\mathbf{V}}$ representing the masses, positions and velocities of the bath variables, and if we further assume that these bath

variables are linearly coupled to the system variables **R**, we obtain a system-bath Hamiltonian,

$$\mathscr{H}_{\mathrm{SB}} = \mathscr{H}_{\mathrm{S}} + \frac{1}{2}\mathrm{Tr}\left[\tilde{\mathbf{V}}^{\mathbf{T}}\tilde{\mathbf{M}}\tilde{\mathbf{V}}\right] + \frac{1}{2}\mathrm{Tr}\left[\left(\mathbf{R}-\tilde{\mathbf{R}}\right)^{\mathbf{T}}\kappa\left(\mathbf{R}-\tilde{\mathbf{R}}\right)\right] \quad (2)$$

where we have introduced the bath kinetic energy, $\frac{1}{2}\mathrm{Tr}[\tilde{\mathbf{V}}^{\mathbf{T}}\tilde{\mathbf{M}}\tilde{\mathbf{V}}]$ and the system-bath coupling is captured by the second term,

$$\frac{1}{2}\mathrm{Tr}\left[\left(\mathbf{R}-\tilde{\mathbf{R}}\right)^{\mathbf{T}}\kappa\left(\mathbf{R}-\tilde{\mathbf{R}}\right)\right] = \frac{1}{2}\mathrm{Tr}\left[\tilde{\mathbf{R}}^{\mathbf{T}}\kappa\tilde{\mathbf{R}}\right] - \mathrm{Tr}\left[\mathbf{R}^{\mathbf{T}}\kappa\tilde{\mathbf{R}} + \tilde{\mathbf{R}}^{T}\kappa\mathbf{R}\right] + \frac{1}{2}\mathrm{Tr}\left[\mathbf{R}^{\mathbf{T}}\kappa\mathbf{R}\right]. \quad (3)$$

Here, κ is a $3N \times 3N$ matrix and both **R** and $\tilde{\mathbf{R}}$ are $3N$ length vectors. Thus, there is potentially one set of bath variables to "drive" each system variable and as noted above, we have combined the harmonic bath term, $\frac{1}{2}\mathrm{Tr}[\tilde{\mathbf{R}}^{\mathbf{T}}\kappa\tilde{\mathbf{R}}]$, the linear system-bath coupling term, $\mathrm{Tr}[-\mathbf{R}^{\mathbf{T}}\kappa\tilde{\mathbf{R}} - \tilde{\mathbf{R}}^{T}\kappa\mathbf{R}]$, and the so-called "counter-term",[6,7] $\frac{1}{2}\mathrm{Tr}[\mathbf{R}^{\mathbf{T}}\kappa\mathbf{R}]$ together into eqn (2). This provides the picture of harmonic force constants κ that connect the system variables, **R** to the bath variables, $\tilde{\mathbf{R}}$. The quantities, κ, also determine the spectral density of the bath degrees of freedom. Eqn (2) represents an ADMP generalization to system bath coupling using the Caldeira–Leggett theory. It is possible to have different values for the three κ terms in eqn (3) but we have found this not to be necessary in our benchmarks in ref. 45.

In ref. 28 and 45 we used eqn (2) to discover the role of active site amino acid groups, specifically ILE-839, in facilitating the hydrogen transfer process. In addition, eqn (2) has also been used in ref. 16 to compute minimum energy paths in the hydrogen transfer step of the oxidation of linoleic acid within SLO-1. In Section IIA we summarize the critical features of ILE-839 participation in the H/D-transfer processes. The precise rationale used in these studies is as follows. The starting point is the hypothesis that it is the fluctuations in the bath variables, $\tilde{\mathbf{R}}$, $\tilde{\mathbf{V}}$, that are in general responsible for rare events being sampled as part of the system subspace dynamics. As a result, in ref. 16, 28 and 45, we bias the initial conditions on $\tilde{\mathbf{R}}$, $\tilde{\mathbf{V}}$ so as to nudge the system along a reaction barrier. Yet again, it is critical to sample over a wide variety of initial conditions before one can compute measurables and infer mechanistic conclusions. This aspect is carefully dealt with in ref. 45.

In Section IIA the role of isoleucine-839 in the H/D transfer process is discussed. In ref. 28 and 45, through the rare events sampling protocols that follow along the lines of ideas discussed above, we find that there exists a positive correlation between a hydrogen bond between ILE-839 and the acceptor hydroxyl group, and the hydrogen transfer event. In Fig. 2 we depict the hydrogen bond between the acceptor-OH and ILE-839 backbone carbonyl group. In Section III we briefly highlight our previous results on probing quantum nuclear effects along these enhanced sampling *ab initio* molecular dynamics (AIMD) trajectory pathways, and then use tensor networks[30] to effectively compute the time-dependent quantum nuclear wavepacket and reaction coordinate-dependent potential surfaces to efficiently represent the associated quantum wavepacket dynamics data. This, we believe, will have a critical role in future steps in studying such problems in large complex assemblies in an efficient manner.

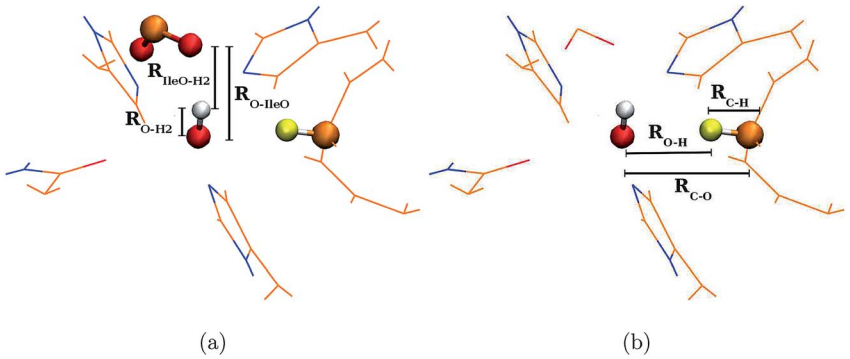

Fig. 2 Part (a) shows the hydrogen bond between the acceptor-OH and ILE-839 backbone carbonyl group, whereas part (b) shows the hydrogen transfer donor acceptor groups.

A. Participation of ILE-839 in the hydrogen transfer process: insights from rare-events sampling

We summarize the critical features that deal with ILE-839 participation in the hydrogen transfer process. Critical simulation details are summarized in Appendix A. Additional details may be found in ref. 28 and 45. Two sets of extensive simulations were conducted. The first was a set of QM/MM (B3LYP/lan12dz:CHARMM) simulations using $\mathscr{H}_{SB}$ as the governing Hamiltonian. This set of calculations included the full enzyme within a QM/MM AIMD study, but with asymptotic boundary conditions. Here an enzyme pocket of size 14 Å, from the iron-cofactor, was allowed to evolve freely as per AIMD; atoms between 14 Å and 16 Å were harmonically constrained; and beyond 16 Å, the system was frozen in dynamics. In all there were 2174 atoms in the QM/MM region that were allowed to evolve freely, and this system is shown in Fig. 3(a). Furthermore, Fig. 3(b) shows the QM/MM classification of the system. Here all parts shown using a ball and stick model are treated with the QM level of theory, whereas everything shown with lines is treated at the MM level. In the next set of simulations, a smaller 50-atom system was carved out from the QM/MM studies for DFT-based AIMD. Through this study, the critical nature of the ILE-839–acceptor-OH hydrogen bond was discovered. This system is shown in Fig. 3(c). We conducted[28] over 400 different classical B3LYP/6-31+G** AIMD biased trajectories spanning a wide range of initial conditions as depicted in Fig. 4(b). For the collection of trajectories in Fig. 4(b), we also note the number of reactive simulations that result in a hydrogen-transfer event, and by extension, the number of non-reactive simulations as well. From the associated collection of hydrogen transfer trajectories we are able to obtain a traditional minimum energy path which is shown in Fig. 4(a). This path is also confirmed[16] through standard techniques available in most electronic structure packages.[52] It may also be noted that while the range of kinetic energies in Fig. 4(b) do coincide with regions of energy above the barrier in Fig. 4(a), the transfer probability does not appear to progress in a monotonic fashion, a reaffirmation of the rare events nature of the reactive process. Furthermore, while some of these effects may arise also from the limited number of AIMD trajectories used here (400 rare-events AIMD simulations, each roughly 1

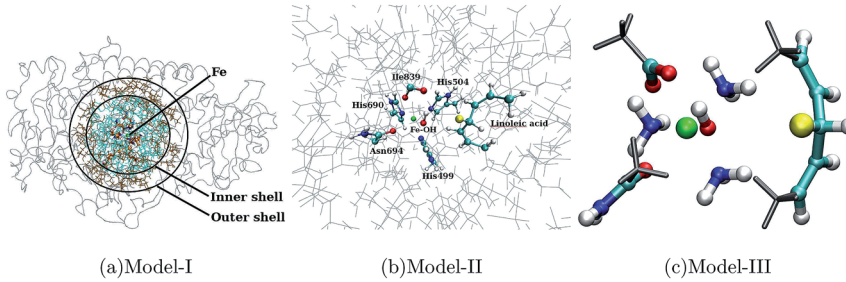

Fig. 3 Model systems of SLO-1 used for the computational validation, and predictions obtained from both classical trajectories calculated using eqn (2) and quantum wavepacket studies constructed on biased trajectories obtained from eqn (2). In ref. 45, Model-I (a), Model-II (b) and Model-III (c) are used to validate the choice of κ as well as initial conditions applied on $\tilde{\mathbf{R}}$ and $\tilde{\mathbf{V}}$. See Appendix A. Furthermore, in ref. 16 and 46, quantum wavepacket dynamics trajectories on the biased trajectories obtained from eqn (2) on Model-III are constructed, using *ab initio* potential surfaces obtained using efficient sampling methods,[47–50] to recover the anomalous kinetic isotope effects noted by Klinman and coworkers.[51] But the complexity of the quantum dynamics calculations reported in ref. 16 is expensive due to the accurate depiction of electron–proton correlations in these studies. Here, in Section III, we present a new method, that utilizes tensor networks to compress this correlation and accurately depict quantum dynamics data such as quantum wavepackets, eigenstates, and potential energy surfaces.

picosecond in length), it is also critical to note from Fig. 4(c) that there exists a sharp divide in the hydrogen bonding propensity between isoleucine-839 and the acceptor OH for productive *versus* non-productive events. Indeed, there appears to be a direct correlation between the propensity of the isoleucine-839–acceptor-OH hydrogen bond and the hydrogen transfer event. This effect, to our knowledge, was shown for the first time in ref. 28 through the set of computationally challenging AIMD simulations using the biased approach discussed in

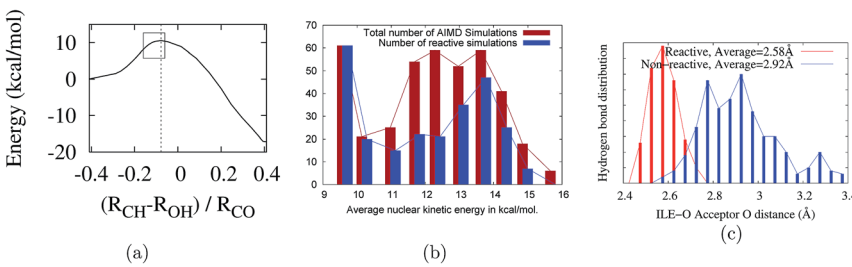

Fig. 4 Part (a) provides the minimum energy reaction profile for the rate-determining hydrogen abstraction step and the critical tunneling region, highlighted within a box, to be discussed in Section III. Part (b) shows the range of initial kinetic energies examined during the 400 different B3LYP/6-31+G** AIMD trajectories, where the number of reactive trajectories in each case is highlighted in blue. Furthermore, for these 400 simulations, part (c) summarizes the role of the ILE-839–acceptor-OH hydrogen bond in promoting the hydrogen transfer process. The hydrogen bond distance distribution is shorter and narrower for the reactive simulations. The figure is obtained from a set of 400 AIMD simulations constructed across SLO-1 active-site primary and secondary (acceptor-OH) isotopologues (see Fig. 2 for an illustration of this secondary hydrogen bond).

Section II. Furthermore, this result holds across four different isotopic substitutions studied in ref. 28 and appears to indicate that the hydrogen bond between the backbone carbonyl belonging to ILE-839 and the acceptor OH may act as a switch in promoting the hydrogen transfer process.

We also find that, when such a hydrogen bond is formed, the acceptor oxygen becomes more electro-negative by a Mulliken charge of about −0.1 a.u. and the donor carbon becomes more electro-positive by about 0.3 a.u. The additional charge is distributed between the transferring proton and the carbonyl oxygen of ILE-839. The evolution of all these charges, averaged over the entire set of productive and non-productive simulations is given in Fig. 5. This net change in charge creates an electric field that appears to drive the transfer process. The extent of this associated perturbative electric field is similar in magnitude to that noted by Boxer and coworkers to power the catalysis in other enzymes.[53]

In the next section we gauge the quantum dynamics of the transferring proton on potential surfaces that are computed along the transfer path (Fig. 4(a)).

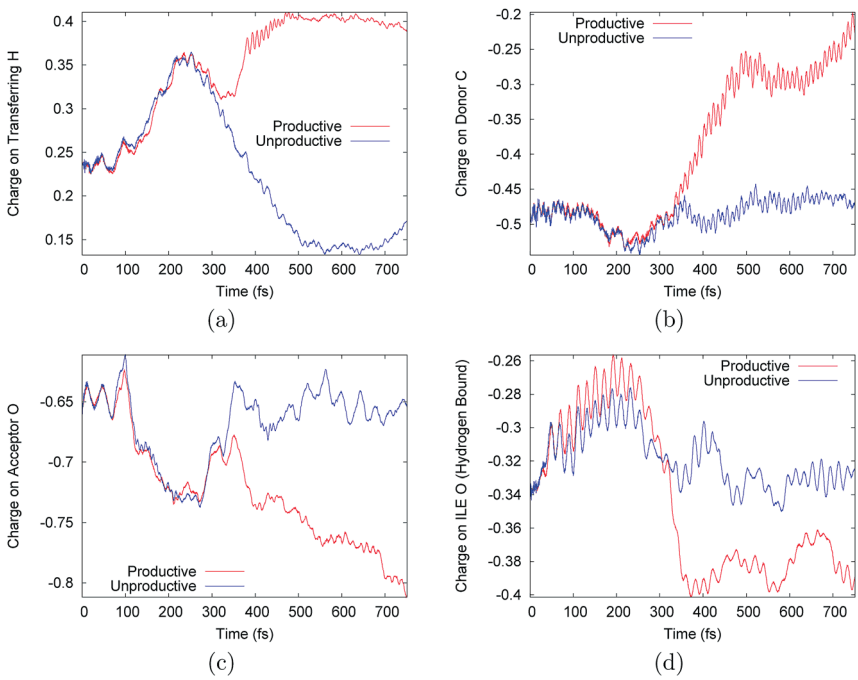

Fig. 5 Evolution of Muliken charge of active site atoms for a typical set of productive and non-productive AIMD simulations: (a) transferring hydrogen (H), (b) acceptor oxygen (O), (c) donor carbon (C_{11}), and (d) the ILE-839-oxygen (IleO). As noted, for the productive simulations (red) the acceptor oxygen acquires a slightly greater negative charge and the donor carbon simultaneously acquires a greater positive charge. The transferring hydrogen, with the acquired greater positive charge, then proceeds towards the acceptor oxygen that is better positioned to accept the hydrogen as a result of its perturbative increase in negative charge. All this, as may be clear from Fig. 4(c), is correlated with the hydrogen bond formed with the backbone oxygen of ILE-839 and hence the associated change in its charge is also noted here.

Furthermore, we present a new approach to compress such quantum dynamics information with the goal of reducing the scaling of such calculations.

III. Representation of electron–proton correlation using tensor networks for nuclear eigenstates, time-dependent wavepackets and potential energy surfaces

In ref. 16, we studied the quantum dynamical evolution of the shared hydrogen/deuterium nuclear degrees of freedom as part of the rate-determining step in the catalytic cycle of the enzyme SLO-1 (Fig. 1). We computed the hydrogen tunneling probabilities for a model system (Fig. 3(c)) constructed from the active site atoms in close proximity to the iron cofactor in SLO-1. This simplification of the active site is based on the assumption that only the immediate environment exerts an electronic influence on the hydrogen transfer. We described the tunneling hydrogen nucleus (proton or deuteron) as a three-dimensional nuclear quantum wavepacket[16,47,48,54–59] coupled to the change in electronic structure that was computed using hybrid density functional theory, benchmarked through MP2 calculations.[16] At each step of the quantum dynamics, the potential surface was obtained by including all electrons in our model system. As a result, the method in ref. 16 is not restricted to a specific mode of transfer such as proton-coupled electron transfer,[11,60] proton transfer, hydrogen transfer or hydride transfer. In addition, the transferring nuclear wavepacket is propagated *via* the time-dependent Schrödinger equation, using an efficient and accurate "distributed approximating functional" propagator.[16,54,55,61,62] Hence all quantum effects pertaining to the quantized H/D nucleus as well as those arising from the electronic degrees of freedom within the model were included. The kinetic isotope effect in ref. 16 was computed by considering a constrained ensemble average of the ratio of transmission probabilities for hydrogen and deuterium. The constraint limits the ensemble average to the portion of the phase space that is sampled during the reactive process. The transmission for each case (H or D) was computed from explicit quantum wavepacket dynamics of the transferring nucleus on potential surfaces obtained from the active site geometry-dependent electronic structure, as highlighted above. Thus, the electronic and quantum nuclear components are both active site geometry-driven, dynamical quantities. Details regarding these quantum dynamical aspects are provided in Appendix B.

The resultant transmission probabilities are shown using the curves in Fig. 6. The black vertical line represents the classical transition state, and as noted both hydrogen and deuterium nuclei show substantial probability transfer prior to the classical transition state. Here, the potential surfaces are computed on a coordinate-space grid, $\bar{x}$, depicting the hydrogen nuclear degrees of freedom, and the propagated wavepacket $\Psi(\bar{x};t) \equiv \Psi(\bar{x},\{\mathbf{R}_\mathbf{C}\};t)$ is explicitly a function of the quantum-nuclear grid representation, $\bar{x}$, but is also parametrically a function of the classical coordinates of atoms belonging to the reaction coordinate, $\mathbf{R}_\mathbf{C}$. As a result, the quantum nuclear degrees of freedom are completely correlated with the change in electronic structure.[57] In this section we provide a method where such correlation can be tailored as required and this approach leads to enormous compression in the amount of quantum nuclear wavefunction data and potential

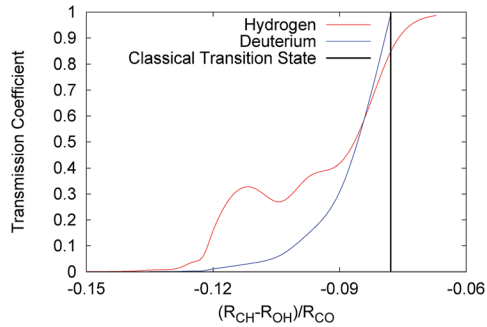

Fig. 6 The transmission probability, when computed using quantum wavepacket dynamics. The black vertical line represents the classical transition state.

surface data, and hence has the potential to greatly reduce the complexity of such quantum dynamics calculations in large systems. We demonstrated the applicability of this approach in ref. 30, to hydrogen transfer reactions of significance to atmospheric chemistry, and here we utilize this approach for the hydrogen transfer rate-determining step in SLO-1.

A. Tensor decomposition of the nuclear wavepacket, potential and eigenstates

We begin by introducing the multi-configurational form of the quantum mechanical wavefunction

$$\begin{aligned}\Psi(\bar{x}) &= \sum_{k_1}\sum_{k_2}\cdots\sum_{k_i}\cdots\sum_{k_{\mathcal{D}}} C_{k_1,k_2,\ldots,k_i,\ldots,k_{\mathcal{D}}}\left[\prod_{i}^{\mathcal{D}}\psi_{i,k_i}(x_i)\right] \\ &= \sum_{\bar{k}} C_{\bar{k}}\left[\prod_{i}^{\mathcal{D}}\psi_{i,k_i}(x_i)\right]\end{aligned} \tag{4}$$

and similarly the potential surface. The quantity $\bar{k}$ is a vector index, with components $\bar{k}\equiv\{k_1, k_2, \ldots, k_i, \ldots, k_{\mathcal{D}}\}$ with k_i being the index to a specific basis function, $\psi_{i,k_i}(x_i)$, along the i^{th} dimension. Similarly, $\bar{x}\equiv\{x_1, x_2, \ldots, x_i, \ldots, x_{\mathcal{D}}\}$. The sum over $\bar{k}$ signifies an independent set of summations over the individual dimensions within $\{k_i\}$ as explicitly indicated. The quantity $C_{\bar{k}}$ in eqn (4) is a tensor of rank $\mathcal{D}$, comprising of $N^{\mathcal{D}}$ elements, where we have assumed, without loss of generality, that there exists N basis elements per dimension.

In ref. 30, eqn (4) is written as a tensor network[31] decomposition, that is,

$$C_{\bar{k}} = \sum_{\bar{\alpha}}\left[\tilde{C}^{1}_{k_1,\alpha_1}\times\left\{\prod_{i=2}^{\mathcal{D}-1}\tilde{C}^{i}_{\alpha_{i-1},k_i,\alpha_i}\right\}\times\tilde{C}^{\mathcal{D}}_{\alpha_{\mathcal{D}-1},k_{\mathcal{D}}}\right] \tag{5}$$

or in turn,

$$\Psi(\bar{x}) = \sum_{\bar{\alpha}}\left[\chi^{1}_{\alpha_1}(x_1)\times\left\{\prod_{i=2}^{\mathcal{D}-1}\chi^{i}_{\alpha_{i-1},\alpha_i}(x_i)\right\}\times\chi^{\mathcal{D}}_{\alpha_{\mathcal{D}-1}}(x_{\mathcal{D}})\right]. \tag{6}$$

This also applies for the potential energy surface:

$$\mathbf{V}(\bar{x}) = \sum_{\bar{\alpha}} \left[\mathcal{V}^{1}_{\alpha_1}(x_1) \times \left\{ \prod_{i=2}^{\mathcal{D}-1} \mathcal{V}^{i}_{\alpha_{i-1},\alpha_i}(x_i) \right\} \times \mathcal{V}^{\mathcal{D}}_{\alpha_{\mathcal{D}-1}}(x_{\mathcal{D}}) \right] \tag{7}$$

and the specific kind of tensor network used in eqn (5)–(7) is called matrix product states (MPS).[31,32,63–65] In ref. 30, we demonstrated the power of this formalism in the study of hydrogen transfer reactions of significance to atmospheric chemistry, but we also introduced additional tensor decoupling approximations,[30] that exploit the system-bath nature of the problem. Here we utilize the above approximations in the study of the hydrogen transfer step in SLO-1. The summation vector index $\bar{\alpha} \equiv \{\alpha_1, \alpha_2, \ldots, \alpha_i, \ldots\}$ in the expressions above. Eqn (5) represents the decomposition of a rank-$\mathcal{D}$ tensor, $C_{\bar{k}}$, into a set of lower rank tensors where, for example, $\tilde{C}_{k_1,\alpha_1}{}^{1}$ is a rank-2 tensor, $\tilde{C}_{\alpha_1,k_2,\alpha_2}{}^{2}$ is a rank-3 tensor, and so on. Similarly in eqn (6) and (7) $\chi_{\alpha_1}{}^{1}(x_1)$, $\{\chi_{\alpha_{i-1},\alpha_i}{}^{i}(x_i)\}$, and $\chi^{\mathcal{D}}_{\alpha_{\mathcal{D}-1}}(x^{0}_{\mathcal{D}})$ and in an analogous manner for the potential surface, $\mathcal{V}^{1}_{\alpha_1}(x_1)$, $\mathcal{V}^{i}_{\alpha_{i-1},\alpha_i}(x_i)$ and $\mathcal{V}^{\mathcal{D}}_{\alpha_{\mathcal{D}-1}}(x_{\mathcal{D}})$ are lower-dimensional (one-dimensional) functions and hence the approach used here provides an adaptive (through iterative singular value decomposition[30]) decomposition of multi-dimensional data into lower dimensions. Specifically, while the full rank $C_{\bar{k}}$ is a tensor of rank $\mathcal{D}$ with $N^{\mathcal{D}}$ elements, the lower rank tensors in eqn (5) include only

$$\mathcal{O}[N \times \{N_\alpha \times [2 + (\mathcal{D} - 2) \times N_\alpha] \equiv \mathcal{O}[N \times N_{\bar{\alpha}}]\}] \tag{8}$$

elements. Here N_α is the maximum value for the summation indices α_i and $N_{\bar{\alpha}} \equiv [2 + (\mathcal{D} - 2) \times N_\alpha]$ is the total summation index for all $\bar{\alpha}$. Furthermore, N_α is an adaptive quantity that is computed on the fly and captures the correlation between dimensions, as necessary. Eqn (8) is potentially linear in N, and in fact as we will see in this paper this approach certainly greatly compresses the amount of information in quantum mechanical wavepackets and potential surfaces and as we will also see, provides a rationale for faster quantum dynamical algorithms. This compression of data arises from the so-called "area-law" of entanglement entropy[31,64,65] where it is noted that most practical systems only occupy a small portion of the exponentially scaling direct-product space that is available to the fully correlated system. Indeed the span of $\bar{\alpha}$ provides us with a measure of the entanglement entropy captured within this algorithm.

B. Adaptively gauging and compressing the extent of correlation in wavefunctions and coupled potentials

The sequential singular value decomposition (SVD) approach provides an adaptive tool to gauge this correlation. The precise nature in which the decomposition above is performed is illustrated here for $C_{\bar{k}}$, but applies to all functions. We begin by treating $C_{\bar{k}}$, which is a rank-$\mathcal{D}$ tensor, as a matrix reshaped such that all trailing dimensions are concatenated, *i.e.*, $C_{\bar{k}} \equiv C_{k_1,(k_2\times\ldots\times k_i\times\ldots\times k_{\mathcal{D}})}$. We next perform a singular value decomposition of $C_{\bar{k}}$ to obtain:

$$C_{\bar{k}} = \sum_{\alpha_1} C^{1}_{k_1,\alpha_1} \times \sigma^{1}_{\alpha_1} \times \mathcal{C}_{\alpha_1,(k_2\times\ldots\times k_i\times\ldots\times k_{\mathcal{D}})} \equiv \sum_{\alpha_1} C^{1}_{k_1,\alpha_1} \times \sigma^{1}_{\alpha_1} \times \mathcal{C}_{\alpha_1,k_2,k_3,\ldots,k_{\mathcal{D}}}. \tag{9}$$

Here, $\{\sigma_{\alpha_1}{}^{1}\}$ are the singular values with associated left and right singular vectors, $\{C_{k_1,\alpha_1}{}^{1}\}$ and $\{\mathcal{C}_{\alpha_1,(k_2\times\ldots\times k_i\times\ldots\times k_{\mathcal{D}})}\}$. In performing the operation in eqn (9) we have recovered a new dimension, α_1, which is interpreted as an internal correlation

dimension since the number of significant α_1 values indicates the deviation of the right side in eqn (9) from a simple product approximation. The tensor, $\mathcal{C}_{\alpha_1,k_2,k_3,\ldots,k_\mathcal{D}}$ is then interpreted (or reshaped) as a matrix:

$$C_{\alpha_1,k_2,k_3,\ldots,k_\mathcal{D}} \equiv C_{(\alpha_1\times k_2),(k_3\times\ldots\times k_i\times\ldots\times k_\mathcal{D})} \tag{10}$$

and carrying out a second singular value decomposition yields:

$$C_{\bar{k}} = \sum_{\alpha_1,\alpha_2} C^1_{k_1,\alpha_1} \times \sigma^1_{\alpha_1} \times C^2_{\alpha_1,k_2,\alpha_2} \times \sigma^2_{\alpha_2} \times \mathcal{C}_{\alpha_2,k_3,k_4,\ldots,k_\mathcal{D}}. \tag{11}$$

Continuing this process $\mathcal{D}-1$ times results in eqn (5) (note that in eqn (5), we have absorbed the $\{\sigma^i_{\alpha_i}\}$ into the C^i and $\tilde{C}^i \equiv \sqrt{\sigma^i_{\alpha_i}} \times C^i$).

Following the same ideas as above, the coordinate space wavefunctions and potentials can be written as

$$\begin{aligned}\Psi(\bar{x}) &= \sum_{\bar{\alpha}}\left[\psi^1_{\alpha_1}(x_1)\times\sigma_{\alpha_1}\left\{\prod_{i=2}^{\mathcal{D}-1}\psi^i_{\alpha_{i-1},\alpha_i}(x_i)\sigma_{\alpha_i}\right\}\times\psi^\mathcal{D}_{\alpha_{\mathcal{D}-1}}(x_\mathcal{D})\right]\\ &= \sum_{\bar{\alpha}}\left[\left(\prod_{i=1}^{\mathcal{D}-1}\sigma_{\alpha_1}\right)\psi^1_{\alpha_1}(x_1)*\left\{\prod_{i=2}^{\mathcal{D}-1}\psi^i_{\alpha_{i-1},\alpha_i}(x_i)\right\}\times\psi^\mathcal{D}_{\alpha_{\mathcal{D}-1}}(x_\mathcal{D})\right]\end{aligned} \tag{12}$$

and similarly,

$$\begin{aligned}\mathbf{V}(\bar{x}) &= \sum_{\bar{\alpha}}\left[\mathcal{V}^1_{\alpha_1}(x_1)\times\tau_{\alpha_1}\left\{\prod_{i=2}^{\mathcal{D}-1}\mathcal{V}^i_{\alpha_{i-1},\alpha_i}(x_i)\tau_{\alpha_i}\right\}\times\mathcal{V}^\mathcal{D}_{\alpha_{\mathcal{D}-1}}(x_\mathcal{D})\right]\\ &= \sum_{\bar{\alpha}}\left[\left(\prod_{i=1}^{\mathcal{D}-1}\tau_{\alpha_1}\right)\mathcal{V}^1_{\alpha_1}(x_1)\times\left\{\prod_{i=2}^{\mathcal{D}-1}\mathcal{V}^i_{\alpha_{i-1},\alpha_i}(x_i)\right\}\mathcal{V}^\mathcal{D}_{\alpha_{\mathcal{D}-1}}(x_\mathcal{D})\right].\end{aligned} \tag{13}$$

From the second expression in eqn (12) and (13) it is clear how the computational reduction and efficiency in storage really materializes. While the coefficients for a fully multi-configurational (that is completely correlated) scheme are tensorial and contain $N^\mathcal{D}$ elements, the coefficients in eqn (12) and (13) contain as many terms as in eqn (8) which could potentially be linear in N if $N_\alpha \ll N$. In practice we find that N_α is a small but non-negligible fraction of N; this certainly is the case for the nuclear wavepackets obtained for the SLO-1 calculations here.

Another interpretation of eqn (12) and (13) is one where a family of direct product bases

$$\mathcal{V}^1_{\alpha_1}(x_1)\otimes\mathcal{V}^2_{\alpha_1,\alpha_2}(x_2)\otimes\mathcal{V}^3_{\alpha_2,\alpha_3}(x_3)\otimes\ldots\otimes\mathcal{V}^i_{\alpha_{\mathcal{D}-1}}(x_\mathcal{D}) \tag{14}$$

and

$$\psi^1_{\alpha_1}(x_1)\otimes\psi^2_{\alpha_1,\alpha_2}(x_2)\otimes\psi^3_{\alpha_2,\alpha_3}(x_3)\otimes\ldots\otimes\psi^i_{\alpha_{\mathcal{D}-1}}(x_\mathcal{D}) \tag{15}$$

are found with coefficients that do not appear to possess the complexity of a fully correlated expansion, since they appear as $(\prod_{i=1}^{\mathcal{D}-1}\sigma_{\alpha_1})$ in eqn (12) and $(\prod_{i=1}^{\mathcal{D}-1}\tau_{\alpha_1})$ in eqn (13). Furthermore, these direct product bases are adaptively determined and the extent of correlation is determined by the size of the set $\bar{\alpha}$. The quantity $\bar{\alpha}$ has also been used in the literature as a measure of the entanglement entropy in the system.[31,64,65]

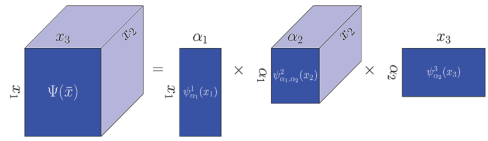

Fig. 7 An illustration of the tensor decomposition in eqn (12) and (13).

The process above is described through illustration in Fig. 7. Three dimensions are considered: $\bar{x} \equiv \{x_1, x_2, x_3\}$, with internal correlator dimensions α_1 and α_2, that are obtained from SVD. Thus, Fig. 7 depicts the transformation:

$$\Psi(x_1, x_2, x_3) = \sum_{\alpha_1, \alpha_2} \left[\psi^1_{\alpha_1}(x_1) \times \sigma_{\alpha_1} \times \psi^2_{\alpha_1, \alpha_2}(x_2) \times \sigma_{\alpha_2} \times \psi^3_{\alpha_2}(x_3) \right]. \tag{16}$$

The singular values, σ_{α_1} and σ_{α_2} are absorbed as part of the one-dimensional functions in the illustration in Fig. 7, as done in eqn (6).

It may also be clear from the above discussion that the decomposition in eqn (11)–(13) is not unique and will change if the dimensions are permuted which may be effected by the order in which the SVD operations are conducted. Ideas similar to eqn (12) and (13) have been used to gauge emerging trends in time-series medical image data[66] and in digital signal processing[67–69] applications. These ideas have also been exploited towards the development of faster MCTDH methods,[70–74] quantum dynamics on a grid much like what is done here[75] and to construct a vibrational approximation to DMRG.[76]

C. Accuracy of eqn (12) and (13) in efficiently representing the SLO-1 potentials, time-dependent wavepackets and hydrogen nuclear eigenstates

For the remaining part of this paper, we provide numerical benchmarks that compare the efficiency and accuracy of the scheme presented above with respect to the quantum wavepacket description in ref. 16. We begin our discussion by analyzing the hydrogen nuclear potential energy surfaces obtained as a function of the reaction coordinate. These potential energy surfaces have a double-well character, where the relative stability of the donor and acceptor side wells changes as the H/D nuclear wavepacket proceeds from donor to acceptor. This may be clear upon inspection of Fig. 8. Furthermore, the curvature of the potential changes both along the donor–acceptor direction as well as in the orthogonal direction. As noted in ref. 16, it was found that the hydrogen and deuterium nuclear wavefunctions were affected by the presence of curve-crossings in the nuclear eigenstate energies along the reaction coordinate. This leads to the dynamics being non-adiabatic[16] in terms of coupling between the hydrogen-transfer dimensions and the larger-scale active site dynamics dimensions. Here we first gauge the accuracy and efficiency of the hydrogen nuclear potential surface representation as a function of the reaction coordinate. Hence, for the discussion here, the potential in eqn (13): $\mathbf{V}(\bar{x}) \equiv \mathbf{V}(\bar{x};\mathbf{R}_C)$, where as noted before, $\bar{x}$ represents the quantum nuclear grid at a given value of the reaction coordinate, $\mathbf{R}_C$.

In Fig. 9 we present the relation between accuracy of the potential (horizontal axis) and data compression (vertical axis). Specifically, the horizontal axis is the

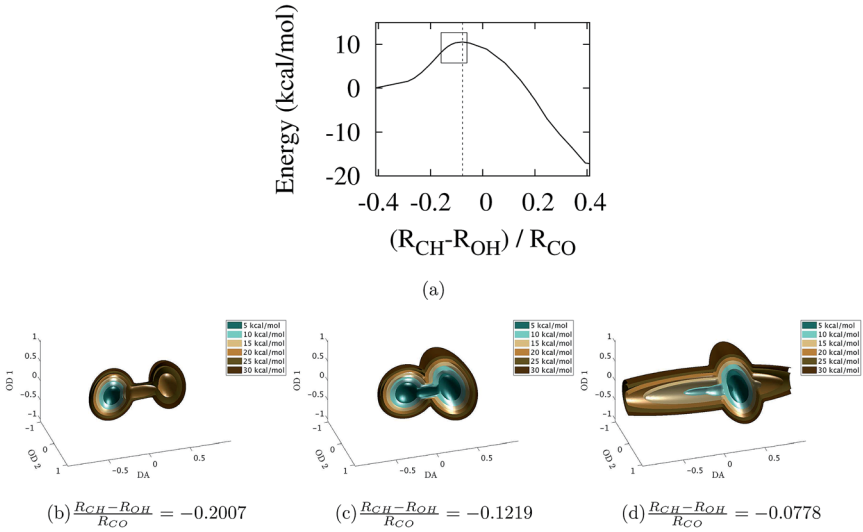

Fig. 8 Fig. 4(a) is reproduced in part (a) for convenience in defining the reaction coordinate and energy profile. In parts (b)–(d), hydrogen nuclear potential surfaces are presented at three different points along the reaction coordinate defined by the horizontal axis in part (a), and the double-well nature of the problem is clear from the relative position and stability of the donor and acceptor side minima. Here R_{CO} is the donor–acceptor coordinate, R_{CH} is the distance between the donor C_{11} and transferring hydrogen and similarly R_{OH} is the distance between the acceptor oxygen and transferring hydrogen nucleus. The potential surfaces in (b)–(d) are obtained on a grid containing 408 321 points for the specific configuration of the active site depicted by the reaction coordinate value. Details are provided in Appendix B.

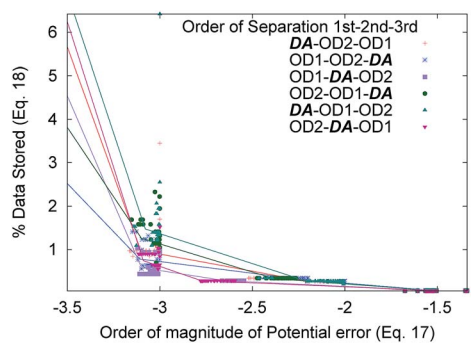

Fig. 9 Accuracy and efficiency in representing the potential energy surfaces as a tensor network. Clearly less than 1% of the grid data needs to be stored to obtain a root-mean-squared error per grid point of 10^{-2} kcal mol^{-1} or a value of $\Gamma_{\mathrm{Err}}{}^{N_a:N_x} = -2$ (which is the horizontal axis here) from eqn (17). All permuted forms of the grid, $\{x_1, x_2, \ldots, x_i, \ldots, x_D\}$, are considered in eqn (13). For example, the donor–acceptor (DA) hydrogen transfer direction may be featured as one of the peripheral directions of the MPS (the keys with DA at the beginning or the end) or the donor–acceptor direction may be the central MPS dimension. In all cases the two orthogonal dimensions (OD1 and OD2) may in turn be permuted and for all permuted sets the compression and accuracies are quite similar.

order of magnitude of the per grid point error where the potential energy is in kcal mol^{-1}:

$$\Gamma_{\mathrm{Err}}^{N_{\bar{\alpha}}:N_{\bar{x}}} \equiv \log_{10}\left(\frac{1}{N_{\bar{x}}}\sqrt{\int \mathrm{d}\bar{x}\left[\mathbf{V}(\bar{x}) - \mathbf{V}_{\mathrm{TN}}^{N_{\bar{\alpha}}:N_{\bar{x}}}(\bar{x})\right]^2}\right). \tag{17}$$

Here $[\mathbf{V}(\bar{x}) - \mathbf{V}_{\mathrm{TN}}{}^{N_{\alpha}:N_{x}}(\bar{x})]$ is the difference between the grid potential discussed above (and in Appendix B) and the tensor network representation of the same, N_{α^-} is defined in eqn (8) and pertains to the total summation index for all α^-(that is the requisite amount of entanglement or correlation between the dimensions of the shared hydrogen nuclear degrees of freedom) and $N_{\bar{x}}$ is the total number of grid points, that is of the order of $N^{\mathcal{D}}$. The vertical axis in Fig. 9 is the percentage of the fraction of the three-dimensional grid that is stored, that is,

$$\text{Fraction of data stored} \equiv \frac{N_{\bar{\alpha}}}{N_{\bar{x}}} \approx \frac{N_{\bar{\alpha}}}{N^{\mathcal{D}}}\frac{[N^{*}\{N_{\alpha}{}^{*}[2+(\mathcal{D}-2)^{*}N_{\alpha}]\}]}{N^{\mathcal{D}}}. \tag{18}$$

Clearly the amount of compression is large and the error is well within the acceptable range. The statistics in Fig. 9 includes all geometries along the reaction coordinate. To further elucidate the method that leads to this level of compression, in Fig. 7 we present the precise set of matrix operations present in the tensor network decomposition. The left side in Fig. 7 is the full grid potential, whereas the right side shows the amount of information that remains after the set of singular value decomposition calculations are completed. Clearly as noted in eqn (13) the extent of data compression is governed by the magnitude of $\left(\prod_{i=1}^{\mathcal{D}-1}\tau_{\alpha_1}\right)$ since, from eqn (13), the 2-norm of the error in the expansion is given by

$$\begin{aligned}\|\mathbf{V}(\bar{x}) - \left\{\sum_{\bar{\alpha}=1}^{N_{\bar{\alpha}}}\left[\left(\prod_{i=1}^{\mathcal{D}-1}\tau_{\alpha_i}\right)\mathcal{V}_{\alpha_1}^{1}(x_1)^{*}\left\{\prod_{i=2}^{\mathcal{D}-1}\mathcal{V}_{\alpha_{i-1},\alpha_i}^{i}(x_i)\right\}\mathcal{V}_{\alpha_{\mathcal{D}-1}}^{\mathcal{D}}(x_{\mathcal{D}})\right]\right\}\| = \\ \|\sum_{\bar{\alpha}=N_{\bar{\alpha}}+1}^{N_{\bar{x}}}\left[\left(\prod_{i=1}^{\mathcal{D}-1}\tau_{\alpha_1}\right)\mathcal{V}_{\alpha_1}^{1}(x_1)^{*}\left\{\prod_{i=2}^{\mathcal{D}-1}\mathcal{V}_{\alpha_{i-1},\alpha_i}^{i}(x_i)\right\}\mathcal{V}_{\alpha_{\mathcal{D}-1}}^{\mathcal{D}}(x_{\mathcal{D}})\right]\|\end{aligned} \tag{19}$$

and this is reflected in Fig. 9. Fig. 10(b) shows the impact of this result. While in Fig. 10(a) we have the full grid potential, Fig. 10(b) shows one direct product function with one-dimensional potentials (see eqn (13)) that model the full grid potential. Of course, the number of one-dimensional potentials is adaptively chosen here based on the desired accuracy.

We now proceed to gauge the behavior of accuracy and efficiency for the ground eigenstates and time-dependent wavepackets. Our results are provided in Fig. 11. In all cases, a 10^{-3} accuracy in the wavepacket and eigenstates can be achieved by only storing 2% of the grid. The effect of this enormous compression is already seen in Fig. 12 where even when 0.05% of data is stored, the qualitative features of transmission are well recovered.

D. Quantum evolution with tensor networks

To efficiently compute the action of the Hamiltonian and quantum time-evolution operator on a wavepacket represented using tensor networks, it is required that kinetic, potential and time-evolution operators independently be

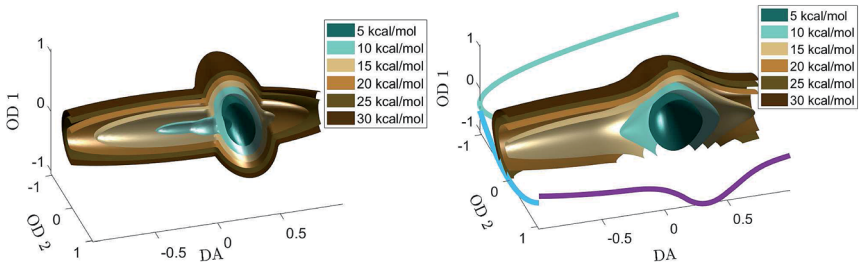

Fig. 10 In part (a) the reduced dimensional hydrogen nuclear potential surface is presented where the left side of the DA axis represents the acceptor state. Part (b) only includes the most significant singular vectors in eqn (13). That is, if $N_\alpha = 1$, the compressed potential would look as in part (b) and this would be a direct product function. The respective one-dimensional basis functions computed from SVD, that is, $\mathcal{V}^1_1(x_1)$, $\mathcal{V}^2_{1,1}(x_2)$ and $\mathcal{V}^3_1(x_3)$ (for $\alpha_1 = \alpha_2 = 1$ in eqn (13)), are shown along the axes lines in part (b). As seen in Section IIIC, including additional SVD basis functions recovers the potential to high accuracy.

described in the same tensor network form. In the previous section we have shown that the potential energy, quantum wavepacket and eigenstates can be written in this form. The kinetic energy operator may always be written as a direct sum over all dimensions and hence the action of the kinetic energy operator on the wavepacket represented in tensorial form rigorously preserves this form at every step according to

$$\begin{aligned}\nabla^2_{\bar{x}}\Phi(\bar{x}) = &\sum_{\bar{\alpha}}\left[\left(\sum_{\kappa'}\tilde{K}^{(2)}(x_1^{\kappa},x_1^{\kappa'})\chi^1_{\alpha_1}(x_1^{\kappa'})\right)\times\left\{\prod_{i=2}^{\mathcal{D}-1}\chi^i_{\alpha_{i-1},\alpha_i}(x_i)\right\}\times\chi^{\mathcal{D}}_{\alpha_{\mathcal{D}-1}}(x_{\mathcal{D}})\right]\\
&+\sum_{\bar{\alpha}}\left[\chi^1_{\alpha_1}(x_1)\times\left(\sum_{\kappa'}\tilde{K}^{(2)}(x_2^{\kappa},x_2^{\kappa'})\chi^2_{\alpha_1,\alpha_2}(x_2^{\kappa'})\right)\right.\\
&\left.\times\left\{\prod_{i=3}^{\mathcal{D}-1}\chi^i_{\alpha_{i-1},\alpha_i}(x_i)\right\}\times\chi^{\mathcal{D}}_{\alpha_{\mathcal{D}-1}}(x_{\mathcal{D}})\right]+\ldots\\
&=\sum_{\bar{\alpha}}\left[\chi^{1,(2)}_{\alpha_1}(x_1)\times\left\{\prod_{i=2}^{\mathcal{D}-1}\chi^i_{\alpha_{i-1},\alpha_i}(x_i)\right\}\times\chi^{\mathcal{D}}_{\alpha_{\mathcal{D}-1}}(x_{\mathcal{D}})\right]\\
&+\sum_{\bar{\alpha}}\left[\chi^1_{\alpha_1}(x_1)\times\chi^{2,(2)}_{\alpha_1,\alpha_2}(x_2)\left\{\prod_{i=3}^{\mathcal{D}-1}\chi^i_{\alpha_{i-1},\alpha_i}(x_i)\right\}\times\chi^{\mathcal{D}}_{\alpha_{\mathcal{D}-1}}(x_{\mathcal{D}})\right]+\ldots\end{aligned}\tag{20}$$

where we have introduced in the second equation, $\chi^{1,(2)}_{\alpha_1}(x_1)\equiv\left(\sum_{\kappa'}\tilde{K}^{(2)}(x_1^{\kappa},x_1^{\kappa'})\chi^1_{\alpha_1}(x_1^{\kappa'})\right)$, $\chi^{2,(2)}_{\alpha_1,\alpha_2}(x_2)\equiv\left(\sum_{\kappa'}\tilde{K}^{(2)}(x_2^{\kappa},x_2^{\kappa'})\chi^2_{\alpha_1,\alpha_2}(x_2^{\kappa'})\right)$ and so on, to exemplify the tensor network form of the second equation. Similarly for free-propagation:

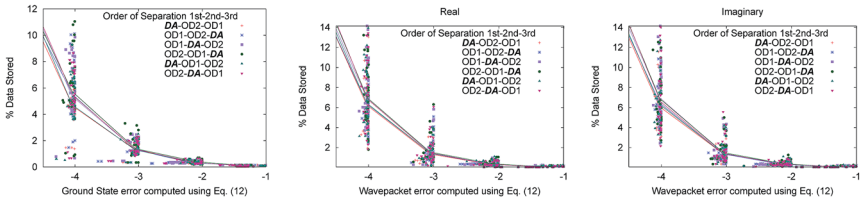

(a)Ground eigenstate (b)Time-dependent wavepacket (c)Time-dependent wavepacket

Fig. 11 Compression of data versus accuracy: part (a) ground eigenstate, (b) and (c) real and imaginary parts of the propagated wavepacket. Multiple matrix product state morphologies have been used and these have the same description as in Fig. 9.

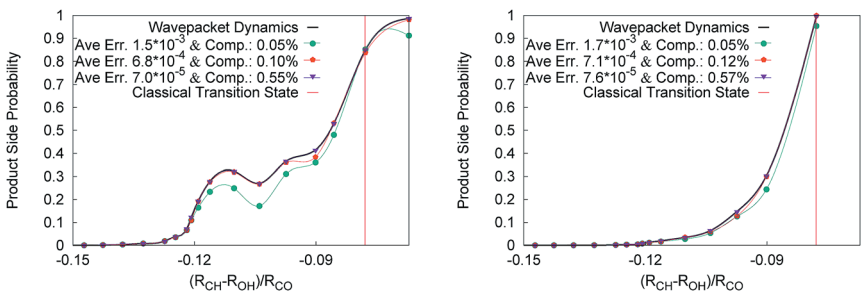

(a)H-tunneling-probability (b)D-tunneling-probability

Fig. 12 The transmission probabilities, (a) hydrogen and (b) deuterium, computed using tensor networks.

$$\begin{aligned}\Phi(\bar{x};t+\Delta t) &= \sum_{\bar{\alpha}}\left[\left(\sum_{\kappa'}\tilde{K}\left(x_1^{\kappa},x_1^{\kappa'};\Delta t\right)\chi^1_{\alpha_1}\left(x_1^{\kappa'};t\right)\right)\right.\\ &\quad\times\left\{\prod_{i=2}^{\mathcal{D}-1}\left(\sum_{\kappa'}\tilde{K}\left(x_i^{\kappa},x_i^{\kappa'};\Delta t\right)\chi^i_{\alpha_{i-1},\alpha_i}\left(x_i^{\kappa'};t\right)\right)\right\}\\ &\quad\left.\times\left(\sum_{\kappa'}\tilde{K}\left(x_{\mathcal{D}}^{\kappa},x_{\mathcal{D}}^{\kappa'};\Delta t\right)\chi^{\mathcal{D}}_{\alpha_{\mathcal{D}-1}}(x_{\mathcal{D}};t)\right)\right]\\ &= \sum_{\bar{\alpha}}\left[\chi^1_{\alpha_1}(x_1;t+\Delta t)\times\left\{\prod_{i=2}^{\mathcal{D}-1}\chi^i_{\alpha_{i-1},\alpha_i}(x_i;t+\Delta t)\right\}\times\chi^{\mathcal{D}}_{\alpha_{\mathcal{D}-1}}(x_{\mathcal{D}};t+\Delta t)\right]\end{aligned} \tag{21}$$

In light of the successful tensor decomposition of the grid potential along the lines of eqn (7) and (13), one may also consider the reduced complexity of the action of the potential energy operator on a wavepacket,

Table 1 Quantum wavepacket grid details

$(R_{CH} - R_{OH})/R_{CO}$	N_{Geom} [a]	N_{Grid} [b]	Grid length
−0.204 through −0.0586[c]	34	81[d] × 71 × 71 = 408 321	2 Å[d] × 2.1 Å × 2.1 Å

[a] Represents the number of active site geometries considered in the range given in column 1. [b] Represents the number of equally spaced proton coordinate grid points utilized to discretize the quantum wavepacket at each active site geometry. [c] The classical transition state occurs at $(R_{CH} - R_{OH})/R_{CO} = -0.0779$ as noted in Fig. 4(a). [d] Donor acceptor axis.

$$\begin{aligned}\int \mathrm{d}\overline{x'}\delta\left(\overline{x}-\overline{x'}\right)\tilde{\mathbf{V}}\left(\overline{x'}\right)\Psi\left(\overline{x'}\right) &= \tilde{\mathbf{V}}(\overline{x})\Psi(\overline{x})\\ &= \sum_{\overline{\alpha},\overline{\beta}}\left\{\mathcal{V}^{1}_{\alpha_1}(x_1)\times\chi^{1}_{\beta_1}(x_1)\right\}\\ &\times\left(\prod_{i=2}^{\mathcal{D}-1}\left\{\mathcal{V}^{i}_{\alpha_{i-1},\alpha_i}(x_i)\times\chi^{i}_{\beta_{i-1},\beta_i}(x_i)\right\}\right)\\ &\times\left\{\mathcal{V}^{\mathcal{D}}_{\alpha_{\mathcal{D}-1}}(x_{\mathcal{D}})\times\chi^{\mathcal{D}}_{\beta_{\mathcal{D}-1}}(x_{\mathcal{D}})\right\}\\ &= \sum_{\overline{\alpha},\overline{\beta}}\chi^{1,V}_{\alpha_1,\beta_1}(x_1)\times\left(\prod_{i=2}^{\mathcal{D}-1}\chi^{i,V}_{\alpha_{i-1},\alpha_i,\beta_{i-1},\beta_i}(x_i)\right)*\chi^{\mathcal{D},V}_{\alpha_{\mathcal{D}-1},\beta_{\mathcal{D}-1}}(x_{\mathcal{D}}).\end{aligned} \tag{22}$$

It is clear upon inspection of this expression that there are $[\beta_1 \times \alpha_1]$ one-dimensional functions created in x_1. Similarly, there are $[\beta_i \times \alpha_i]$ one-dimensional functions created in x_i, thus presenting a potential increase in the number of such one-dimensional functions. But we also note, as per eqn (5) and (7) that the singular values have been absorbed into the one-dimensional functions and hence, we expect the contributions from the higher product singular values to progressively reduce. These aspects will be probed in future publications.

IV. Conclusion

We consider the rate-determining step in the catalytic oxidation of linoleic acid by soybean lipoxygenase-1. This step involves a hydrogen transfer process that shows a large primary kinetic isotope effect, $k_H/k_D = 81$. From a computational standpoint there are two main bottlenecks that deeply affect the accurate simulation of such processes. On the one hand, while the hydrogen transfer process may occur in the pico-second time-scale, the actual reorganization of the enzyme active site that affects this process is, statistically speaking a rare event. We present two methods in this paper to address such processes.

First, rare events sampling is incorporated into *ab initio* molecular dynamics by starting from a Caldeira–Leggett system-bath Hamiltonian. Here the proton-transfer system is linearly coupled to a harmonic bath and this Hamiltonian is also a starting point in the derivation of other spin-Boson-type Hamiltonians used in quantum dissipative theory. Using an *ab initio* molecular dynamics generalization of the Caldeira–Leggett system-bath Hamiltonian, we probe the reactive hydrogen-transfer event and discuss the role of ILE-839 as a switch in modulating

the transfer event. We find that the formation of the hydrogen bond between the backbone carbonyl group of ILE-839 and the acceptor hydroxyl group is positively correlated with the hydrogen transfer process.

After providing a computationally efficient approach to rare event sampling, that incorporates on-the-fly *ab initio* potentials, we next consider the hydrogen transfer process using quantum wavepacket dynamics. While the wavepacket dynamics procedure is able to recover the large isotope effect accurately, using on-the-fly *ab initio* potentials, the exponential scaling nature of quantum dynamics hinders the routine application of such rigorous methods. Here we utilize a tensor-network form of the quantum wavepacket and potential surface to present the quantum dynamics problem using tensor networks. We gauge the accuracy of storage of quantum wavepackets and of potential energy surfaces and find that tensor networks are an efficient and accurate option for the representation and propagation of quantum dynamics data.

Appendix A. Simulation details for rare events sampling

Details regarding the parameters used in the rare events dynamics simulations are presented in ref. 28 and 45. We summarize the critical aspects here for completeness. In ref. 45, Model-I, Model-II and Model-III in Fig. 3 are used to validate the choice of κ as well as initial conditions applied on $\tilde{\mathbf{R}}$ and $\tilde{\mathbf{V}}$. In ref. 45, a monotonic sequence of decreasing values for κ and initial conditions on $\tilde{\mathbf{V}}$ are used to test the validity of these parameters. In ref. 28, these parameters are used and in the process the role of ILE-839 is elucidated in providing a control, or a switch, for the hydrogen transfer process. In summary the donor (carbon), the acceptor (oxygen) and the transferring proton (see Fig. 2) were tethered to bath particles, referred to as $\tilde{\mathbf{R}}$ in eqn (2), where the respective constraint harmonic force constant values captured within κ are chosen to be 15 570 pN Å^{-1}. The force constants used here are commensurate with those in other rare events sampling studies[5,77] and in the atomic force microscopy literature.[78] In units more commonly used in chemistry, 15 570 pN Å^{-1} ~224.0965 kcal mol^{-1} Å^{-2}. This harmonic force constant corresponds to a frequency ($\bar{\nu}$) of about 450 cm^{-1} on the carbon and oxygen atoms and roughly 1500 cm^{-1} on the transferring hydrogen. These frequencies are estimated using the relation between force constant and frequency: $\kappa = 4\pi^2 c^2 m \bar{\nu}^2$ where c is the velocity of light, m is the mass of the particle in question and $\bar{\nu}$ is the frequency in cm^{-1}. Consistent with the requirement of heavier bath particles to allow greater sampling of the system during rare event sampling, the masses for the bath particles tethered to donor and acceptor are 500 amu whereas the degrees of freedom tethered to the transferring hydrogen have a mass of 100 amu in our study. Detailed benchmarks on these parameters can be found in ref. 45.

Appendix B. Simulation details for quantum wavepacket dynamics calculations conducted along the reaction coordinate

In ref. 16, the quantum dynamics of the H/D transferring nucleus, represented as a wavepacket, evolves under the influence of reaction coordinate-dependent

potentials, $\mathbf{V}(\bar{x};\mathbf{R}_C)$, where the quantum mechanical free-propagator is approximated in the coordinate representation using the distributed approximating functional propagator (DAF):[55,61,62]

$$\tilde{K}_k(x_i,x_j;t) = \frac{1}{\sigma(0)\sqrt{2\pi}}\left(\frac{-1}{\sqrt{2}\sigma(0)}\right)^k \exp\left(-\frac{(x_i-x_j)^2}{2\sigma(t)^2}\right) \times \sum_{n=0}^{M/2}\left(\frac{\sigma(0)}{\sigma(t)}\right)^{2n+1}\left(\frac{-1}{4}\right)^n \frac{1}{n!}H_{2n+k}\left(\frac{x_i-x_j}{\sqrt{2}\sigma(t)}\right). \quad \text{(B1)}$$

The terms H_{2n+k} are Hermite polynomials and $\sigma(t)^2 = \sigma(0)^2 + \imath\hbar t/m$.[55] Eqn (B1) represents a formally exact representation of the quantum dynamical free-propagator[55,61,62] for $k = 0$ and finite t, whereas it also serves as accurate derivative operator functions known on a grid when k is chosen to be the order of the derivative and t is set to zero. Details regarding the properties of eqn (B1) are discussed in several publications.[55,61,62,79–81] The variables M and $\sigma(0)$ determine the accuracy and width respectively of the DAF. It has been shown[54,55,61,82] that these parameters are not independent and for a given value of M there exists a $\sigma(0)$ that provides optimal accuracy for the propagation. The accuracy of this method in conjunction with *ab initio* dynamics has been benchmarked in ref. 48, 54 and 57–59. As discussed in previous publications,[54,57,58,61,62] calculations are performed for $M = 60$ and $\frac{\sigma(0)}{\Delta x} = 2.5742$. This provides a good compromise between accuracy and efficiency. Furthermore, to allow efficient calculation of the Hermite polynomials in eqn (B1), the recursion relations are modified to allow the direct evaluation of

$$\tilde{H}_{2n}\left(\frac{x}{\sqrt{2}\sigma}\right) = \exp\left\{-\frac{x^2}{2\sigma^2}\right\}\frac{1}{n!}H_{2n}\left(\frac{x}{\sqrt{2}\sigma}\right), \quad \text{(B2)}$$

using

$$\tilde{H}_{2n}(y) = \frac{2}{n}\left[(2y^2-4n+3)\tilde{H}_{2n-2}(y) - 4(2n-3)\tilde{H}_{2n-4}(y)\right]. \quad \text{(B3)}$$

Eqn (B3) only includes the even or odd polynomials as needed in eqn (B1). This modified recursion allows numerically stable evaluation of the components required in eqn (B1) even for very large values of M.

The quantum dynamical evolution of the wavepacket is constructed using Trotter factorization.[83,84] The grid description for the quantum wavepacket is given in Table 1. The transmission amplitude is computed using the total probability density of the time-dependent wavepacket on the product-side of the proton potential energy surface at each time step. Product-side functions are taken as a Heaviside function and these aspects are along the lines of the calculations discussed in ref. 30 and 50. Using this approach the kinetic isotope effect was computed in ref. 16 with results that agree with the large KIE reported by Klinman and coworkers.[85]

The potentials are computed on the grid described in Table 1. Details can be found in ref. 16 and a summary is given here. All electrons in the active site model

are treated together using DFT and MP2. In Table 1 we provide a list of geometries or range of geometries (column 1) characterized by values of the reaction coordinate described in Fig. 4(a), the number of geometries considered inside each range (column 2) and the number of proton coordinate grid points utilized to discretize the wavepacket for each active site geometry (column 3). The origin of the proton coordinate grid space is taken to be the center of the donor–acceptor distance. The three-dimensional Cartesian grid is oriented such that one axis is along the donor–acceptor line and a second axis is oriented along the plane comprising the donor carbon, the acceptor oxygen and the hydrogen bonded to the donor carbon. The third axis is orthogonal to the plane comprising the other axes.

The electronic structure calculations required for constructing the proton potential surface at each model system geometry were performed using the B3LYP density functional and lanl2dz Gaussian-type basis set. The choice of functional and basis set was based on a comparison of the proton potential energy surfaces and eigenstates obtained at different levels of theory including MP2. The benchmark data for DFT and MP2 are provided in the Appendix in ref. 16. It was found that the B3LYP density functional and lanl2dz basis provided acceptable accuracy at a limited computational expense. All calculations are performed using a development version of the Gaussian series of electronic structure programs.[86] Furthermore, due to the large computational overhead involved in obtaining the full potential surface,[47,48] we enforced the following approximations: we first computed the proton potential surfaces for seven geometries in the range described in Table 1 by performing approximately 5000 B3LYP/lanl2dz electronic structure calculations at each of the seven geometries. The energies obtained from these calculations were then interpolated to an extremely fine grid of over a million points *via* Hermite curve interpolation.[47,48,87–89] We then compared these potential surfaces to an approximate surface generated by: (a) computing the energy, gradients and Hessian for cases where the transferring hydrogen was donor-bound, acceptor-bound and at the transition state for each of the seven geometries (b) and then constructing a smooth double well potential by interpolating between two harmonic curves centered on the donor and acceptor minima with curvatures determined from *ab initio* force constants. The interpolating function is a Gaussian parameterized to reproduce the *ab initio* barrier height. The full *ab initio* surfaces for the seven geometries described above were compared with the more approximate surface for a description of the localization properties of the low-lying eigenstates in all three directions. Since the comparisons were found to be adequate with good qualitative agreement, we chose to use the approximate surfaces for each geometry described in Table 1.

Conflicts of interest

To the best of my knowledge we do not have any conflict of interest.

Acknowledgements

This research is supported by the National Science Foundation grant NSF CHE-1665336 to SSI. Author ND also gratefully acknowledges support from the Kenneth Kratz Family Charitable Foundation.

References

1 *Hydrogen-Transfer Reactions*, ed. J. T. Hynes, J. P. Klinman, H.-H. Limbach and R. L. Schowen, Wiley-VCH, Weinheim, Germany, 2007.
2 N. Isaacs, *Physical Organic Chemistry*, Longman Scientific and Technical, Essex, 1995.
3 R. Sheridan, Quantum Mechanical Tunneling in Organic Reactive Intermediates, in *Reviews of Reactive Intermediate Chemistry*, ed. M. Platz, R. A. Moss and J. Maitland Jones, Wiley-Interscience, Hoboken, NJ, 2007.
4 C. Jarzynski, Nonequilibrium Equality for Free Energy Differences, *Phys. Rev. Lett.*, 1997, **78**, 2690.
5 S. Park, F. Khalili-Araghi, E. Tajkhorshid and K. Schulten, Free Energy Calculation from Steered Molecular Dynamics Simulations Using Jarzynski's Equality, *J. Chem. Phys.*, 2003, **119**, 3559.
6 A. O. Caldeira and A. J. Leggett, Quantum tunnelling in a dissipative system, *Ann. Phys.*, 1983, **149**, 374–456.
7 A. J. Leggett, S. Chakravarty, A. T. Dorsey, M. P. A. Fisher, A. Garg and W. Zwerger, Dynamics of the dissipative two-state system, *Rev. Mod. Phys.*, 1987, **59**, 1–85.
8 Z. X. Liang and J. P. Klinman, Structural Bases of Hydrogen Tunneling in Enzymes: Progress and Puzzles, *Curr. Opin. Struct. Biol.*, 2004, **14**, 648.
9 M. H. Glickman, J. S. Wiseman and J. P. Klinman, Extremely Large Isotope Effects in the Soybean Lipoxygenase-Linoleic Acid Reaction, *J. Am. Chem. Soc.*, 1994, **116**, 793.
10 N. Lehnert and E. I. Solomon, Density-Functional Investigation on the Mechanism of H-atom Abstraction by Lipoxygenase, *J. Biol. Inorg Chem.*, 2003, **8**, 294.
11 E. Hatcher, A. V. Soudackov and S. Hammes-Schiffer, Proton-Coupled Electron Transfer in Soybean Lipoxygenase, *J. Am. Chem. Soc.*, 2004, **126**, 5763.
12 M. H. M. Olsson, P. E. M. Siegbahn and A. Warshel, Simulations of the Large Kinetic Isotope Effect and the Temperature Dependence of the Hydrogen Atom Transfer in Lipoxygenase, *J. Am. Chem. Soc.*, 2004, **126**, 2820.
13 M. H. M. Olsson, P. E. M. Siegbahn and A. Warshel, Density-Functional Investigation on the Mechanism of H-atom Abstraction by Lipoxygenase, *J. Biol. Inorg Chem.*, 2004, **9**, 96.
14 J. Mavri, H. Liu, M. H. M. Olsson and A. Warshel, Simulation of Tunneling in Enzyme Catalysis by Combining a Biased Propagation Approach and the Quantum Classical Path Method: Application to Lipoxygenase, *J. Phys. Chem. B*, 2008, **112**, 5950.
15 W. Siebrand and Z. Smedarchina, Temperature Dependence of Kinetic Isotope Effects for Enzymatic Carbon-Hydrogen Bond Cleavage, *J. Phys. Chem. B*, 2004, **108**, 4185.
16 S. S. Iyengar, I. Sumner and J. Jakowski, Hydrogen Tunneling in an Enzyme Active Site: A Quantum Wavepacket Dynamical Perspective, *J. Phys. Chem. B*, 2008, **112**, 7601.
17 I. Tejero, M. Garcia-Viloca, A. Gonzalez-Lafont, J. M. Lluch and D. M. York, Enzyme Dynamics and Tunneling Enhanced by Compression in the

Hydrogen Abstraction Catalyzed by Soybean Lipoxygenase, *J. Phys. Chem. B*, 2006, **110**, 24708.

18 S. Hu, A. R. Offenbacher, E. M. Thompson, C. L. Gee, J. Wilcoxen, C. A. M. Carr, D. M. Prigozhin, V. Yang, T. Alber, R. D. Britt, J. S. Fraser and J. P. Klinman, Biophysical Characterization of a Disabled Double Mutant of Soybean Lipoxygenase: The "Undoing" of Precise Substrate Positioning Relative to Metal Cofactor and an Identified Dynamical Network, *J. Am. Chem. Soc.*, 2019, **141**, 1555–1567.

19 J. P. Klinman, A. R. Offenbacher and S. Hu, Origins of Enzyme Catalysis: Experimental Findings for C-H Activation, New Models, and Their Relevance to Prevailing Theoretical Constructs, *J. Am. Chem. Soc.*, 2017, **139**, 18409–18427.

20 S. Hu, A. V. Soudackov, S. Hammes-Schiffer and J. P. Klinman, Enhanced Rigidification within a Double Mutant of Soybean Lipoxygenase Provides Experimental Support for Vibronically Nonadiabatic Proton-Coupled Electron Transfer Models, *ACS Catal.*, 2017, **7**, 3569–3574.

21 A. V. Soudackov and S. Hammes-Schiffer, Probing Nonadiabaticity in the Proton-Coupled Electron Transfer Reaction Catalyzed by Soybean Lipoxygenase, *J. Phys. Chem. Lett.*, 2014, **5**, 3274–3278.

22 P. Li, A. V. Soudackov and S. Hammes-Schiffer, Fundamental Insights into Proton-Coupled Electron Transfer in Soybean Lipoxygenase from Quantum Mechanical/Molecular Mechanical Free Energy Simulations, *J. Am. Chem. Soc.*, 2018, **140**, 3068–3076.

23 P. Li, A. V. Soudackov and S. Hammes-Schiffer, Impact of Mutations on the Binding Pocket of Soybean Lipoxygenase: Implications for Proton-Coupled Electron Transfer, *J. Phys. Chem. Lett.*, 2018, **9**, 6444–6449.

24 B. Salna, A. Benabbas, D. Russo and P. M. Champion, Tunneling Kinetics and Nonadiabatic Proton-Coupled Electron Transfer in Proteins: The Effect of Electric Fields and Anharmonic Donor-Acceptor Interactions, *J. Phys. Chem. B*, 2017, **121**, 6869–6881.

25 S. Hammes-Schiffer, Proton-Coupled Electron Transfer: Moving Together and Charging Forward, *J. Am. Chem. Soc.*, 2015, **137**, 8860–8871.

26 M. E. Newcomer and A. R. Brash, The structural basis for specificity in lipoxygenase catalysis, *Protein Sci.*, 2015, **24**, 298–309.

27 M. Horitani, A. R. Offenbacher, C. A. M. Carr, T. Yu, V. Hoeke, G. E. Cutsail, S. Hammes-Schiffer, J. P. Klinman and B. M. Hoffman, ^{13}C ENDOR Spectroscopy of Lipoxygenase-Substrate Complexes Reveals the Structural Basis for C-H Activation by Tunneling, *J. Am. Chem. Soc.*, 2017, **139**, 1984–1997.

28 P. Phatak, J. Venderley, J. Debrota, J. Li and S. S. Iyengar, Active Site Dynamical Effects That Facilitate the Hydrogen Transfer Process in Soybean Lipoxygenase-1 (SLO-1): Isotope Effects, *J. Phys. Chem. B*, 2015, **119**, 9532.

29 K. W. Rickert and J. P. Klinman, Nature of Hydrogen Transfer in Soybean Lipoxygenase 1: Separation of Primary and Secondary Isotope Effects, *Biochemistry*, 1999, **38**, 12218.

30 N. DeGregorio and S. S. Iyengar, Adaptive dimensional decoupling for compression of quantum nuclear wavefunctions and efficient potential energy surface representations through tensor network decomposition, *J. Chem. Theory Comput.*, 2019, **15**, 2780.

31 R. Orús, A practical introduction to tensor networks: matrix product states and projected entangled pair states, *Ann. Phys.*, 2014, **349**, 117–158.
32 G. K.-L. Chan, A. Keselman, N. Nakatani, Z. Li and S. R. White, Matrix product operators, matrix product states, and *ab initio* density matrix renormalization group algorithms, *J. Chem. Phys.*, 2016, **145**, 014102.
33 R. Car and M. Parrinello, Unified Approach for Molecular Dynamics and Density-Functional Theory, *Phys. Rev. Lett.*, 1985, **55**, 2471.
34 H. B. Schlegel, J. M. Millam, S. S. Iyengar, G. A. Voth, A. D. Daniels, G. E. Scuseria and M. J. Frisch, *Ab Initio* Molecular Dynamics: Propagating the Density Matrix with Gaussian Orbitals, *J. Chem. Phys.*, 2001, **114**, 9758.
35 S. S. Iyengar, H. B. Schlegel, J. M. Millam, G. A. Voth, G. E. Scuseria and M. J. Frisch, *Ab Initio* Molecular Dynamics: Propagating the Density Matrix with Gaussian Orbitals. II. Generalizations Based on Mass-Weighting, Idempotency, Energy Conservation and Choice of Initial Conditions, *J. Chem. Phys.*, 2001, **115**, 10291.
36 H. B. Schlegel, S. S. Iyengar, X. Li, J. M. Millam, G. A. Voth, G. E. Scuseria and M. J. Frisch, *Ab Initio* Molecular Dynamics: Propagating the Density Matrix with Gaussian Orbitals. III. Comparison with Born-Oppenheimer Dynamics, *J. Chem. Phys.*, 2002, **117**, 8694.
37 S. S. Iyengar, H. B. Schlegel, G. A. Voth, J. M. Millam, G. E. Scuseria and M. J. Frisch, *Ab Initio* Molecular Dynamics: Propagating the Density Matrix with Gaussian Orbitals. IV. Formal Analysis of the Deviations from Born-Oppenheimer Dynamics, *Isr. J. Chem.*, 2002, **42**, 191.
38 S. S. Iyengar and M. J. Frisch, Effect of Time-Dependent Basis Functions and Their Superposition Error on Atom-Centered Density Matrix Propagation (ADMP): Connections to Wavelet Theory of Multi-Resolution Analysis, *J. Chem. Phys.*, 2004, **121**, 5061.
39 N. Rega, S. S. Iyengar, G. A. Voth, H. B. Schlegel, T. Vreven and M. J. Frisch, Hybrid *Ab Initio*/Empirical Molecular Dynamics: Combining the ONIOM Scheme with the Atom-Centered Density Matrix Propagation (ADMP) Approach, *J. Phys. Chem. B*, 2004, **108**, 4210.
40 J. Li, C. Haycraft and S. S. Iyengar, Hybrid, Extended Lagrangian – Born-Oppenheimer *Ab Initio* Molecular Dynamics using Fragment-Based Electronic Structure, *J. Chem. Theory Comput.*, 2016, **12**, 2493.
41 J. Li and S. S. Iyengar, *Ab initio* Molecular Dynamics using Recursive, Spatially Separated, Overlapping Model Subsystems Mixed Within an ONIOM Based Fragmentation Energy Extrapolation Technique, *J. Chem. Theory Comput.*, 2015, **11**, 3978–3991.
42 C. Haycraft, J. Li and S. S. Iyengar, "On-the-fly" *Ab initio* molecular dynamics with coupled cluster accuracy, *J. Chem. Theory Comput.*, 2017, **13**, 21887.
43 T. C. Ricard, C. Haycraft and S. S. Iyengar, Adaptive, geometric networks for efficient coarse-grained *ab initio* molecular dynamics with post-Hartree-Fock accuracy, *J. Chem. Theory Comput.*, 2018, **14**, 2852.
44 T. C. Ricard and S. S. Iyengar, Efficiently capturing weak interactions in *ab initio* molecular dynamics through "on-the-fly" basis set extrapolation, *J. Chem. Theory Comput.*, 2018, **14**, 5535.
45 P. Phatak, I. Sumner and S. S. Iyengar, Gauging the Flexibility of the Active Site in Soybean Lipoxygenase-1 (SLO-1) Through an Atom-Centered Density Matrix

Propagation (ADMP) Treatment That Facilitates the Sampling of Rare Events, *J. Phys. Chem. B*, 2012, **116**, 10145.

46 I. Sumner and S. S. Iyengar, Analysis of Hydrogen Tunneling in an Enzyme Active Site Using Von Neumann Measurements, *J. Chem. Theory Comput.*, 2010, **6**, 1698.

47 J. Jakowski, I. Sumner and S. S. Iyengar, Computational Improvements to Quantum Wavepacket *Ab Initio* Molecular Dynamics Using a Potential-Adapted, Time-Dependent Deterministic Sampling Technique, *J. Chem. Theory Comput.*, 2006, **2**, 1203.

48 I. Sumner and S. S. Iyengar, Quantum Wavepacket *Ab Initio* Molecular Dynamics: An Approach for Computing Dynamically Averaged Vibrational Spectra Including Critical Nuclear Quantum Effects, *J. Phys. Chem. A*, 2007, **111**, 10313.

49 D. Hocker, X. Li and S. S. Iyengar, Shannon Information Entropy Based Time-Dependent Deterministic Sampling Techniques for Efficient "on-The-Fly" Quantum Dynamics and Electronic Structure, *J. Chem. Theory Comput.*, 2011, **7**, 256.

50 N. DeGregorio and S. S. Iyengar, Efficient and Adaptive Methods for Computing Accurate Potential Surfaces for Quantum Nuclear Effects: Applications to Hydrogen-Transfer Reactions, *J. Chem. Theory Comput.*, 2018, **14**, 30–47.

51 M. H. Glickman, J. S. Wiseman and J. P. Klinman, Extremely Large Isotope Effects in the Soybean Lipoxygenase-Linoleic Acid Reaction, *J. Am. Chem. Soc.*, 1994, **116**, 793.

52 M. J. Frisch, G. W. Trucks, H. B. Schlegel, G. E. Scuseria, M. A. Robb, J. R. Cheeseman, G. Scalmani, V. Barone, B. Mennucci, G. A. Petersson, H. Nakatsuji, M. Caricato, X. Li, H. P. Hratchian, A. F. Izmaylov, J. Bloino, G. Zheng, J. L. Sonnenberg, M. Hada, M. Ehara, K. Toyota, R. Fukuda, J. Hasegawa, M. Ishida, T. Nakajima, Y. Honda, O. Kitao, H. Nakai, T. Vreven, J. A. Montgomery Jr, J. E. Peralta, F. Ogliaro, M. Bearpark, J. J. Heyd, E. Brothers, K. N. Kudin, V. N. Staroverov, T. Keith, R. Kobayashi, J. Normand, K. Raghavachari, A. Rendell, J. C. Burant, S. S. Iyengar, J. Tomasi, M. Cossi, N. Rega, J. M. Millam, M. Klene, J. E. Knox, J. B. Cross, V. Bakken, C. Adamo, J. Jaramillo, R. Gomperts, R. E. Stratmann, O. Yazyev, A. J. Austin, R. Cammi, C. Pomelli, J. W. Ochterski, R. L. Martin, K. Morokuma, V. G. Zakrzewski, G. A. Voth, P. Salvador, J. J. Dannenberg, S. Dapprich, P. V. Parandekar, N. J. Mayhall, A. D. Daniels, O. Farkas, J. B. Foresman, J. V. Ortiz, J. Cioslowski and D. J. Fox, *Gaussian Development Version, Revision H.37+*, Gaussian, Inc., Wallingford CT, 2010.

53 S. D. Fried, S. Bagchi and S. G. Boxer, Extreme electric fields power catalysis in the active site of ketosteroid isomerase, *Science*, 2014, **346**, 1510–1514.

54 S. S. Iyengar and J. Jakowski, Quantum Wavepacket *Ab Initio* Molecular Dynamics: An Approach to Study Quantum Dynamics in Large Systems, *J. Chem. Phys.*, 2005, **122**, 114105.

55 S. S. Iyengar, *Ab Initio* Dynamics with Wave-Packets and Density Matrices, *Theor. Chem. Acc.*, 2006, **116**, 326.

56 I. Sumner and S. S. Iyengar, Combining Quantum Wavepacket *Ab Initio* Molecular Dynamics (QWAIMD) with QM/MM and QM/QM Techniques:

Implementation Blending ONIOM and Empirical Valence Bond Theory, *J. Chem. Phys.*, 2008, **129**, 054109.

57 X. Li and S. S. Iyengar, Quantum Wavepacket *Ab Initio* Molecular Dynamics: Generalizations Using an Extended Lagrangian Treatment of Diabatic States Coupled Through Multi-Reference Electronic Structure, *J. Chem. Phys.*, 2010, **133**, 184105.

58 J. Li, X. Li and S. S. Iyengar, Vibrational Properties of Hydrogen Bonded Systems Using the Multi-Reference Generalization to the "On-The-Fly" Electronic Structure Within Quantum Wavepacket *Ab Initio* Molecular Dynamics (QWAIMD), *J. Chem. Theory Comput.*, 2014, **10**, 2265.

59 A. H. Prociuk and S. S. Iyengar, A Multi-Wavelet Treatment of the Quantum Subsystem in Quantum Wavepacket *Ab Initio* Molecular Dynamics Through an Hierarchical Partitioning of Momentum Space, *J. Chem. Theory Comput.*, 2014, **10**, 2950.

60 E. Hatcher, A. V. Soudackov and S. Hammes-Schiffer, Proton-Coupled Electron Transfer in Soybean Lipoxygenase: Dynamical Behavior and Temperature Dependence of Kinetic Isotope Effects, *J. Am. Chem. Soc.*, 2007, **129**, 187.

61 D. K. Hoffman, N. Nayar, O. A. Sharafeddin and D. J. Kouri, Analytic Banded Approximation for the Discretized Free Propagator, *J. Phys. Chem.*, 1991, **95**, 8299.

62 D. J. Kouri, Y. Huang and D. K. Hoffman, Iterated Real-Time Path Integral Evaluation Using a Distributed Approximating Functional Propagator and Average-Case Complexity Integration, *Phys. Rev. Lett.*, 1995, **75**, 49.

63 U. Schollwöck, The density-matrix renormalization group in the age of matrix product states, *Ann. Phys.*, 2011, **326**, 96–192, Special Issue.

64 J. Eisert, M. Cramer and M. B. Plenio, Colloquium: Area laws for the entanglement entropy, *Rev. Mod. Phys.*, 2010, **82**, 277–306.

65 L. Accardi, Topics in quantum probability, *Phys. Rep.*, 1981, **77**, 169–192.

66 P. P. Kanjilal, S. Palit and G. Saha, Fetal ECG extraction from single-channel maternal ECG using singular value decomposition, *IEEE Trans. Biomed. Eng.*, 1997, **44**, 51–59.

67 H. Hassanpour, A time-frequency approach for noise reduction, *Digit. Signal Process.*, 2008, **18**, 728–738.

68 N. Iqbal, A. Zerguine, S. Kaka and A. Al-Shuhail, Automated SVD filtering of time-frequency distribution for enhancing the SNR of microseismic/microquake events, *J. Geophys. Eng.*, 2016, **13**, 964.

69 C. Hu, X. Lu, M. Ye and W. Zeng, Singular value decomposition and local near neighbors for face recognition under varying illumination, *Pattern Recognit.*, 2017, **64**, 60–83.

70 H.-D. Meyer, U. Manthe and L. S. Cederbaum, The Multi-Configurational Time-Dependent Hartree Approach, *Chem. Phys. Lett.*, 1990, **165**, 73.

71 H. Wang and M. Thoss, Multilayer formulation of the multiconfiguration time-dependent Hartree theory, *J. Chem. Phys.*, 2003, **119**, 1289–1299.

72 D. Peláez and H.-D. Meyer, The multigrid POTFIT (MGPF) method: Grid representations of potentials for quantum dynamics of large systems, *J. Chem. Phys.*, 2013, **138**, 014108.

73 A. Leclerc and T. Carrington, Calculating vibrational spectra with sum of product basis functions without storing full-dimensional vectors or matrices, *J. Chem. Phys.*, 2014, **140**, 174111.

74 F. Otto, Multi-layer Potfit: an accurate potential representation for efficient high-dimensional quantum dynamics, *J. Chem. Phys.*, 2014, **140**, 014106.
75 S. M. Greene and V. S. Batista, Tensor-Train Split-Operator Fourier Transform (TT-SOFT) Method: Multidimensional Nonadiabatic Quantum Dynamics, *J. Chem. Theory Comput.*, 2017, **13**, 4034–4042.
76 A. Baiardi, C. J. Stein, V. Barone and M. Reiher, Vibrational Density Matrix Renormalization Group, *J. Chem. Theory Comput.*, 2017, **13**, 3764–3777.
77 S. Park and K. Schulten, Calculating Potentials of Mean Force from Steered Molecular Dynamics Simulations, *J. Chem. Phys.*, 2004, **120**, 5946.
78 W. R. Bowen, R. W. Lovitt and C. J. Wright, Application of Atomic Force Microscopy to the Study of Micromechanical Properties of Biological Materials, *Biotechnol. Lett.*, 2000, **22**, 893.
79 C. Chandler and A. Gibson, Uniform Approximation of Functions with Discrete Approximation Functionals, *J. Approx. Theory*, 1999, **100**, 233.
80 G. W. Wei, S. C. Althorpe, D. J. Kouri and D. K. Hoffman, An Application of Distributed Approximating Functional-Wavelets to Reactive Scattering, *J. Chem. Phys.*, 1998, **108**, 7065.
81 S. S. Iyengar, G. A. Parker, D. J. Kouri and D. K. Hoffman, Symmetry-Adapted Distributed Approximating Functionals: Theory and Application to the Ro-Vibrational States of H_3^+, *J. Chem. Phys.*, 1999, **110**, 10283.
82 D. K. Hoffman, M. Arnold and D. J. Kouri, Properties of the Optimum Distributed Approximating Function Class Propagator for Discretized and Continuous Wave Packet Propagations, *J. Phys. Chem.*, 1992, **96**, 6539.
83 M. F. Trotter, On the Product of Semi-Groups of Operators, *Proc. Am. Math. Soc.*, 1959, **10**, 545.
84 E. Nelson, Feynman Integrals and the Schrödinger Equation, *J. Math. Phys.*, 1964, **5**, 332.
85 Z. Nagel and J. Klinman, Tunneling and Dynamics in Enzymatic Hydride Transfer, *Chem. Rev.*, 2006, **106**, 3095.
86 M. J. Frisch, G. W. Trucks, H. B. Schlegel, G. E. Scuseria, M. A. Robb, J. R. Cheeseman, J. A. Montgomery Jr, T. Vreven, K. N. Kudin, J. C. Burant, J. M. Millam, S. S. Iyengar, J. Tomasi, V. Barone, B. Mennucci, M. Cossi, G. Scalmani, N. Rega, G. A. Petersson, H. Nakatsuji, M. Hada, M. Ehara, K. Toyota, R. Fukuda, J. Hasegawa, M. Ishida, T. Nakajima, Y. Honda, O. Kitao, H. Nakai, M. Klene, X. Li, J. E. Knox, H. P. Hratchian, J. B. Cross, C. Adamo, J. Jaramillo, R. Gomperts, R. E. Stratmann, O. Yazyev, A. J. Austin, R. Cammi, C. Pomelli, J. W. Ochterski, P. Y. Ayala, K. Morokuma, G. A. Voth, P. Salvador, J. J. Dannenberg, V. G. Zakrzewski, S. Dapprich, A. D. Daniels, M. C. Strain, O. Farkas, D. K. Malick, A. D. Rabuck, K. Raghavachari, J. B. Foresman, J. V. Ortiz, Q. Cui, A. G. Baboul, S. Clifford, J. Cioslowski, B. B. Stefanov, G. Liu, A. Liashenko, P. Piskorz, I. Komaromi, R. L. Martin, D. J. Fox, T. Keith, M. A. Al-Laham, C. Y. Peng, A. Nanayakkara, M. Challacombe, P. M. W. Gill, B. Johnson, W. Chen, M. W. Wong, C. Gonzalez and J. A. Pople, *Gaussian Development Version, Revision B.01*, Gaussian, Inc., Pittsburgh PA.
87 S. Carter, J. M. Bowman and B. J. Braams, On Using Low-Order Hermite Interpolation in 'direct Dynamics' Calculations of Vibrational Energies Using the Code 'MULTIMODE', *Chem. Phys. Lett.*, 2001, **342**, 636.

88 K. M. Christoffel, J. M. Bowman and B. J. Braams, A Local Interpolation Method for Direct Classical Dynamics Calculations, *J. Chem. Phys.*, 2001, **115**, 11021.

89 R. H. Bartels, J. C. Beatty and B. A. Barsky, *An Introduction to Splines for Use in Computer Graphics and Geometric Modeling*, Morgan Kaufman Publishers, Inc., Los Altos, California, 1987.